Room Temperature Ferromagnetic Ordering from Bound Magnetic Polarons in Rare Earth Doped Ultrathin MoS_2 Nanosheets

Eng Tuan Poh[^], Rajasree Das[^], Manikandan Marimuthu[^], Zheng Zhang[#], Ramanathan Mahendiran[^*], Chorng Haur Sow[^*]

[^] Department of Physics, National University of Singapore, 2 Science Drive 3, Singapore 117551

[#]Institute of Materials Research and Engineering, A*STAR (Agency for Science, Technology and Research), Singapore 138634

[*]Address correspondence to
Prof. Chorng Haur Sow. Tel: (+65) 65162957. E-mail: physowch@nus.edu.sg
A/Prof. Ramanathan Mahendiran. Tel: +(65) 65162616. Email: phyrm@nus.edu.sg

Keywords: Molybdenum Disulphide, Nanosheets, Lanthanide, Rare Earth, Ferromagnetism

Abstract

Dilute magnetic semiconductors (DMS) imbued with room temperature ferromagnetic capabilities that arise from bound magnetic polarons (BMPs) have been attractive for spintronics, information storage and magneto-optical applications. In particular, the inclusion of rare-earth lanthanide ions as magnetic dopants in semiconductors presents significant potential owing to their strong free ion magnetic moments. Here, we evaluate the influence of various rare earth dopants (Tb^{3+}, Er^{3+}, Eu^{3+}) magnetically coupled to vacancy carrier spins in MoS_2 nanosheets. The manifested ferromagnetic magnitudes adopt a trend that differs from that of the free ion moments, with 5% Tb-doped MoS_2 presenting a maximum saturation magnetization. The characteristic dependence of sample magnetization upon dopant concentration and annealing stringency (defect concentration) justifies the BMP model in describing the system. The rational creation of these ferromagnetic nanosheets is expected to provide value in low temperature, solution-based processing of spintronic components into monolithic integrated electronics and multifunctional devices. These findings are also expected to shape extensive understanding towards the design of rare earth doped transition metal dichalcogenides (TMDs) as DMS for such future spintronic applications.

1. Introduction

Since the initial predictions of room temperature ferromagnetic properties in dilute magnetic semiconductors (DMS),[1,2] the incessant trials across a glossary of dopant and host combinations have prompted continual research efforts in the domain. At low doping concentrations, the acquired ferromagnetic magnitudes in these systems have subverted the withstanding notions of magnetism physics. It is expected that short-range interactions in conventional super-exchange and double-exchange processes are incapable of explaining the long-range magnetic order from such low-density distribution of magnetic inclusions. Only with the subsequent proposals involving bound magnetic polarons (BMP),[3–8] was a reasonable model available to account for the magnetic performance conferred to DMSs involving wide bandgap semiconductor hosts embedded with transition metal (TM)[9–12] and rare-earth dopants.

The subsequent surge in experimental explorations initiated many nano-systems inclusive of Mn-doped CdX (X = S, Se, Te),[13,14] $CaMn_7O_{12}$,[15] Ce-doped $BaTiO_3$,[16] Co-doped Dy_2O_3[17] and M-doped ZnO (M = Yb,[18] Mn,[19] Tb,[20] Eu,[21] Co,[22,23] Cu,[24] Ni,[25] Sm[26]), each with magnetic characteristics befitting of the BMP theory. Furthermore, with massive research attention invested into semiconducting 2D transition metal dichalcogenides (TMDs) in recent years, the ensuing studies on doped TMDs with various nanostructure morphologies have expanded tremendously. Across a multitude of transition metals, including Zn,[27] Mn,[28–31] Fe,[32–34] Co,[35–38] Cu[39,40] and V[41–46] emplaced amidst matrices of TMD nanostructures, the evoked magnetic properties in such doped nano-systems were experimentally verified against various models. More importantly, subsequent theoretical predictions[47,48] were in favor of thermodynamic substitution of lanthanide ions in MoS_2, prompting targeted modulation in the optical and magnetic properties by doping. Amidst the meagre quantities of lanthanide-doped MoS_2 literatures available, the majority revolved around Er and Eu dopants studied across a diverse range of optical (NIR-related),[49–54] thermometry[55] and photoelectric[56,57] applications. Only a handful evaluated the ferromagnetic performances in MoS_2 nanosheets arising from lanthanide doping, chiefly from Nd[58], Dy[59] and Ho[60,61] induced BMP formation.

Piqued by the scarce availability of works assessing the magnetic capability of rare earth doped MoS_2 nanosheets, the current work presents a systematic analysis of the magnetic influence from representative lanthanide ions (Terbium (Tb), Europium (Eu) and Erbium (Er)) doped into MoS_2 nanosheets. Leveraging upon the expected abundance of vacancy defects in the nanosheets, we anticipate different magnetic anisotropies for the respective ions amid the crystal host lattice with varying extents of BMP interaction. Across low doping concentrations (up to 8%), the resultant ferromagnetic ordering was indeed dependent upon nanosheet quality, dopant variant and doping concentrations, with exceptional fitting statistics in accordance with the BMP model. The acquired ferromagnetic transitions and Curie temperatures near room temperature further validated the potential of lanthanide-doped nanosheets as DMS for room temperature spintronics, in correspondence with preceding theoretical expectations.

Furthermore, with ever-increasing involvement of 2D materials in the development of advanced micro and nanoelectronics owing to the diversified electronic properties of its members,[62–65] the production of solution-based TMD nanosheets have prompted potential for mass producing printed electronics via low temperature processing technologies.[66–69] It is imperative to evaluate the capability to induce a magnetic response in MoS_2 nanosheets through a convenient and scalable doping processes, so as to develop the technology as a magnetic or

spintronic component to be integrated into multifunctional devices and monolithic integrated electronics.[70–72] The advantage of functionalized nanosheet inks to produce printed layer stacks without the need for orthogonal considerations, coupled with the ease to flexibly alter the nanosheet properties, will encourage seamless integration of multifunctional and flexible printed electronics.

2. Experimental Section

2.1. Chemicals

Ammonium thiomolybdate ($(NH_4)_2MoS_4$, 99.97%), Dimethylformamide (DMF, 99.8%), Isopropanol (IPA, 99.5%) and rare earth lanthanide chloride salts: Terbium (III) chloride ($TbCl_3 \cdot 6H_2O$, 99.9%), Erbium (III) chloride ($ErCl_3 \cdot 6H_2O$, 99.9%) and Europium (III) chloride ($ErCl_3 \cdot 6H_2O$, 99.9%) are all purchased from Sigma Aldrich. All chemicals are used without further purification or processing steps.

2.2. Synthesis of Lanthanide-doped MoS_2 Nanosheets

Dark red crystals of $(NH_4)_2MoS_4$ (6.67 mg; 0.025 mmol) were sonicated in DMF (12 mL) until a homogeneous red solution was obtained. Aqueous stock solutions of the various lanthanide salts ($TbCl_3$, $ErCl_3$, $EuCl_3$) were prepared prior (2.5 mM), with the appropriate quantity (depending on respective atomic doping %, detailed calculations and solution volumes utilized are presented under Table S1) withdrawn and added into the red thiomolybdate solution above. The resultant mix was sonicated before transferring into a Teflon-lined stainless-steel autoclave. The resultant suspension was heated in the oven at 200°C for 15 hours. After the autoclave was allowed to cool naturally to room temperature, the dark precipitate obtained was isolated by centrifugation before repeated procedures of redispersion-centrifugation washes in a DMF (4 mL)/IPA (11 mL) solvent pair. The resultant lanthanide-doped MoS_3 nanosheets were redispersed in IPA (4 mL) and dried overnight in the oven at 80°C. The subsequent annealing step was conducted in a tube furnace (850-900°C, 2 hours) under different conditions (inert Ar; Ar with air) to afford crystalline lanthanide-doped MoS_2 nanosheets.

2.3. Physical Characterization

Raman spectra were obtained from Renishaw inVia 2000 Micro-Raman spectrometer equipped with a 532 nm laser. SEM images with the corresponding EDX spectra were acquired from a JEOL JSM-6700F field emission scanning electron microscope (FESEM) operated at 15 kV, under Secondary Electron Imaging (SEI) with a chamber pressure of 9.63×10^{-5} Pa. The system is coupled with an Oxford Instruments X-Max^N 150 EDX detector. HRTEM and TEM measurements were acquired from a JEOL-JEM 3010 field emission transmission electron microscope operating at 200 kV acceleration voltage under a chamber pressure of 3×10^{-8} Pa. XPS elemental analyses were conducted using a Thermo Fisher Scientific Theta Probe XPS system. Magnetic measurements were performed using a PPMS tagged to a Lakeshore model 7404 VSM.

3. Results and Discussion

3.1. Characterization of Lanthanide Doped Nanosheets

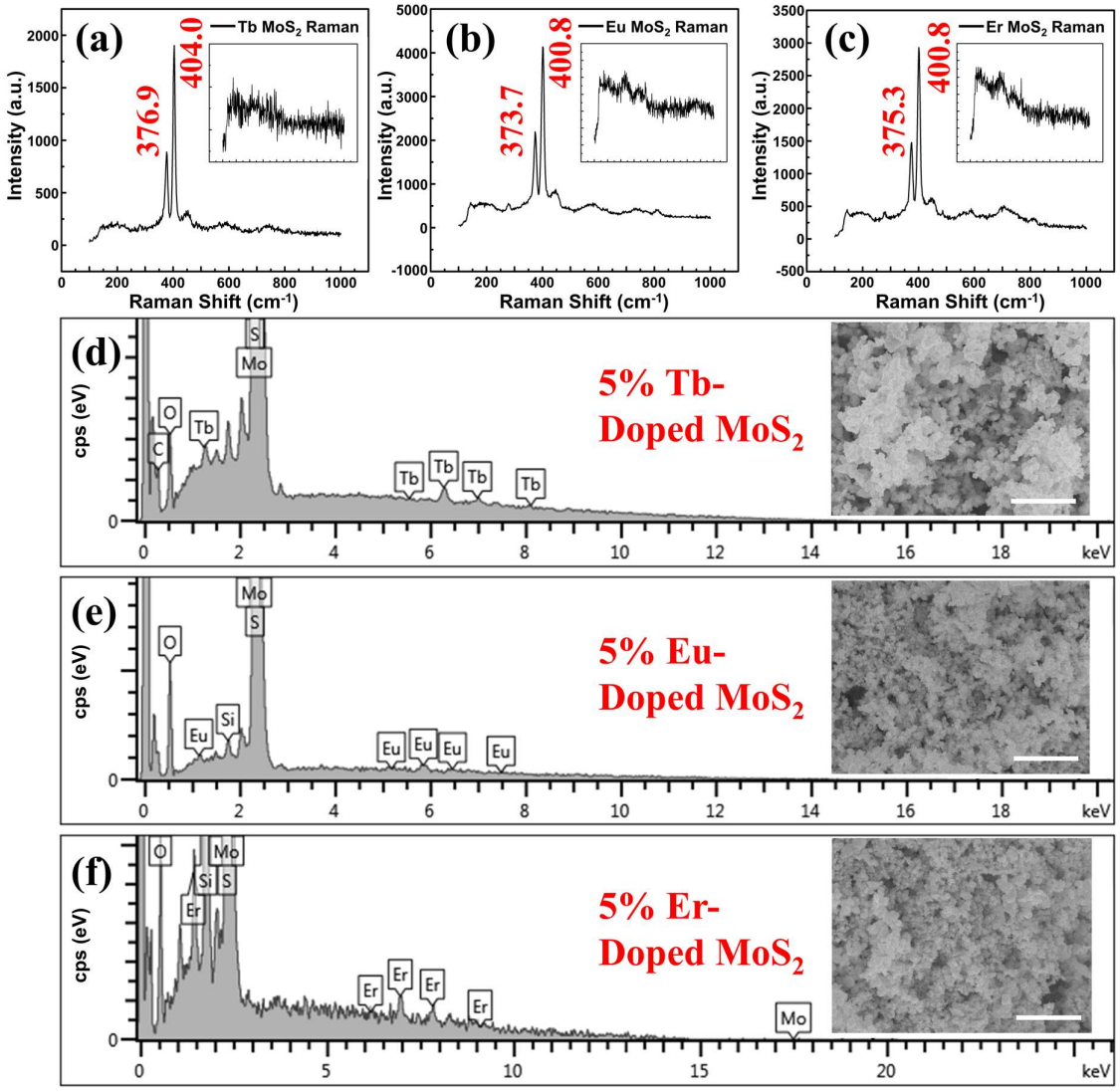

Figure 1. Raman and SEM-EDX characterization of Ln-doped MoS_2 nanosheets. (a – c) Raman spectra of the respective Ln-doped MoS_2 nanosheets acquired under 532 nm excitation: **(a)** Tb-doped MoS_2 **(b)** Eu-doped MoS_2 **(c)** Er-doped MoS_2. **Inset**: Corresponding Raman spectra of pre-formed Ln-doped MoS_3 nanosheets prior to annealing: Tb-doped MoS_3, Eu-doped MoS_3 and Er-doped MoS_3. **(d – f)** EDX elemental profile of Ln-doped MoS_2 (Ln = **(d)** Tb, **(e)** Eu, **(f)** Er) at 5% atomic doping. **Inset:** Respective SEM images of the annealed nanosheets. (Scale bars = 10 μm)

The lanthanide doped nanosheets herein were synthesized through a two-step hydrothermal-annealing process involving an intermediate amorphous MoS_3 state. Spiked with small quantities of lanthanide chlorides ($LnCl_3$; Ln = Tb, Eu, Er), ammonium thiomolybdate was broken down to yield Ln-doped MoS_3 nanosheets, prior to a subsequent high temperature annealing to form crystalline MoS_2. **Figure 1a-c** presents the Raman signals of the as-produced MoS_2 nanosheets characterized by the distinct E_{2g} and A_{1g} vibrational modes,[73,74] contrasting

against the relatively featureless profile of the pre-annealed amorphous MoS_3 forms[75] **(Figure 1a-c insets)**. This marks the successful conversion under optimal annealing conditions with no alternate magnetic phase (1T-MoS_2)[76] or oxidized (MoO_3 or MoO_xS_y) side-products. With SEM-EDX, the nanosheet morphology of the MoS_2 samples **(Figure 1d-f insets)** was ascertained, with the successful incorporation of these selected *f*-block dopants (Tb^{3+}, Er^{3+}, Eu^{3+}) verified via the presence of its corresponding elemental signals **(Figure 1d-f)**.

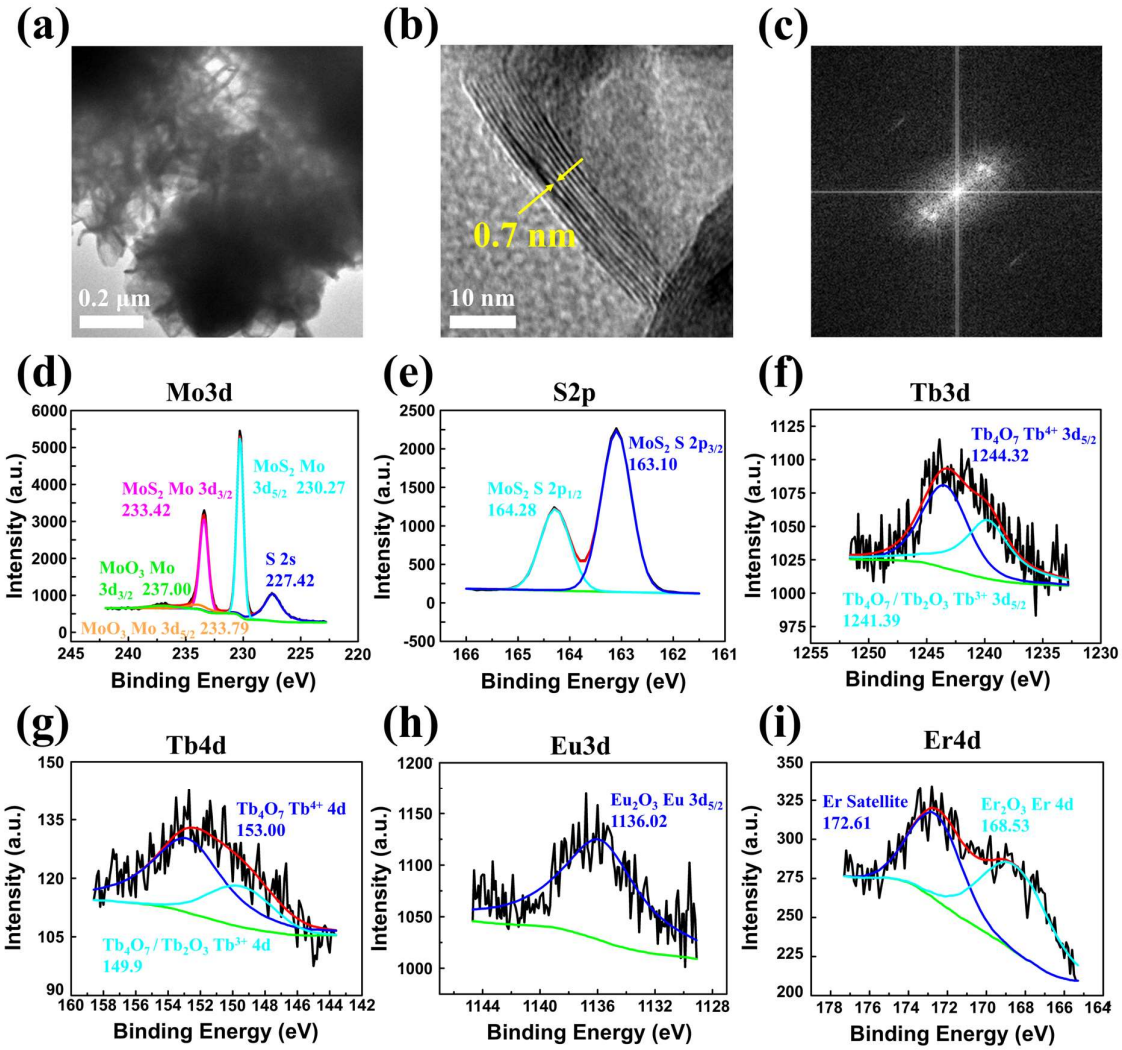

Figure 2. TEM characterization and XPS analyses of Ln-doped MoS_2 nanosheets. (a) Representative low magnification TEM image of Ln-doped MoS_2 nanosheet clusters. **(b)** Representative HRTEM of Ln-doped MoS_2 nanosheets detailing the 0.7 nm interlayer stacking. **(c)** Corresponding SAED pattern. **(d, e)** Representative XPS spectra of **(d)** Mo3d and **(e)** S2p composition in the Ln-doped nanosheets. **(f – i)** Elemental signals for **(f)** Tb3d, **(g)** Tb4d, **(h)** Eu3d and **(i)** Er4d for the respective variants of Ln-doped nanosheets.

Under scrutiny from HRTEM imaging **(Figure 2a-c)**, the nanosheet cluster revealed multilayer stacks comprising an expected 0.7 nm interlayer spacing; an observation coherent with the wide Raman inter-peak separation (E_{2g}, A_{1g}) typical of multilayer samples **(Figure 1a-c)**. Similar nanostructure morphologies and interlayer spacings across various samples **(Figure S1)** assured the consistency and reproducibility of the nanosheet synthesis process, along with no

obvious clustering of the rare-earth ions. Complementary to EDX, the indication of successful lanthanide doping was corroborated by detailed XPS analysis. As shown in **Figure 2d** and **2e**, the Mo3d and S2p elemental signals displayed clean spectrums with prominent $Mo3d_{5/2}$ – $Mo3d_{3/2}$ and $S2p_{3/2}$ – $S2p_{1/2}$ doublet pairs. The absence of MoS_3 related peaks (S_2^{2-} and bridging S peaks for S2p; MoS_3 peaks for Mo3d; **Figure S2**) affirmed a complete conversion after the annealing step, while the lack of any impurity-related signals assures the nanosheet quality. The absence of signals associated with any magnetically active Mo^{5+} species (spin ½, B.E. 234 eV) ensures no ferromagnetic interference from any Mo^{5+} components.[77] Comparatively, the similar peak distributions and intensity ratios for the Mo3d and S2p spectra across all three samples (Ln = Tb, Eu, Er) affirms high sample consistency **(Figure S3)**.

Meanwhile, the discernible lanthanide signals confirmed the presence of the dopants (Tb^{3+}, Eu^{3+}, Er^{3+}) within disparate chemical environments in the samples. Interestingly, terbium ions doped into the nanosheets adopt dual oxidation states, comprising Tb^{3+} and Tb^{4+}. The XPS peaks were mapped in similar correspondence to mixed oxidations in Tb_4O_7 (Tb^{3+}, Tb^{4+})[78–80] and Tb_2O_3/TbO_2 (Tb^{3+}, Tb^{4+})[81–83] analogues **(Figure 2f,g)**. While it may be intuitively understandable that a redox conversion from Tb^{3+} ion to the Tb^{4+} state should allow greater thermodynamic stability for substitution at the Mo^{4+} site, discussions relating to such possibilities are typically not addressed in preceding computational investigations and may warrant further studies. On the contrary, without the option of a stable +4 oxidation state, the erbium and europium dopants were unsurprisingly found to be prominent in the trivalent states **(Figure 2h,i)**, with the respective distinct signals of $Eu3d_{5/2}$ and Er4d at 1136.0 eV and 168.5 eV. Furthermore, an additional peak for erbium at 172.6 eV can be assigned to Er satellite signal **(Figure 2i)**. Coherently, the results of EDX and XPS measurements ascertained the identity of the nanosheets formed, along with the presence of the respective dopants, effectively substantiating the successful formation of the proposed nanosheet formulations.

3.2. Magnetic Performance of Lanthanide Doped Nanosheets

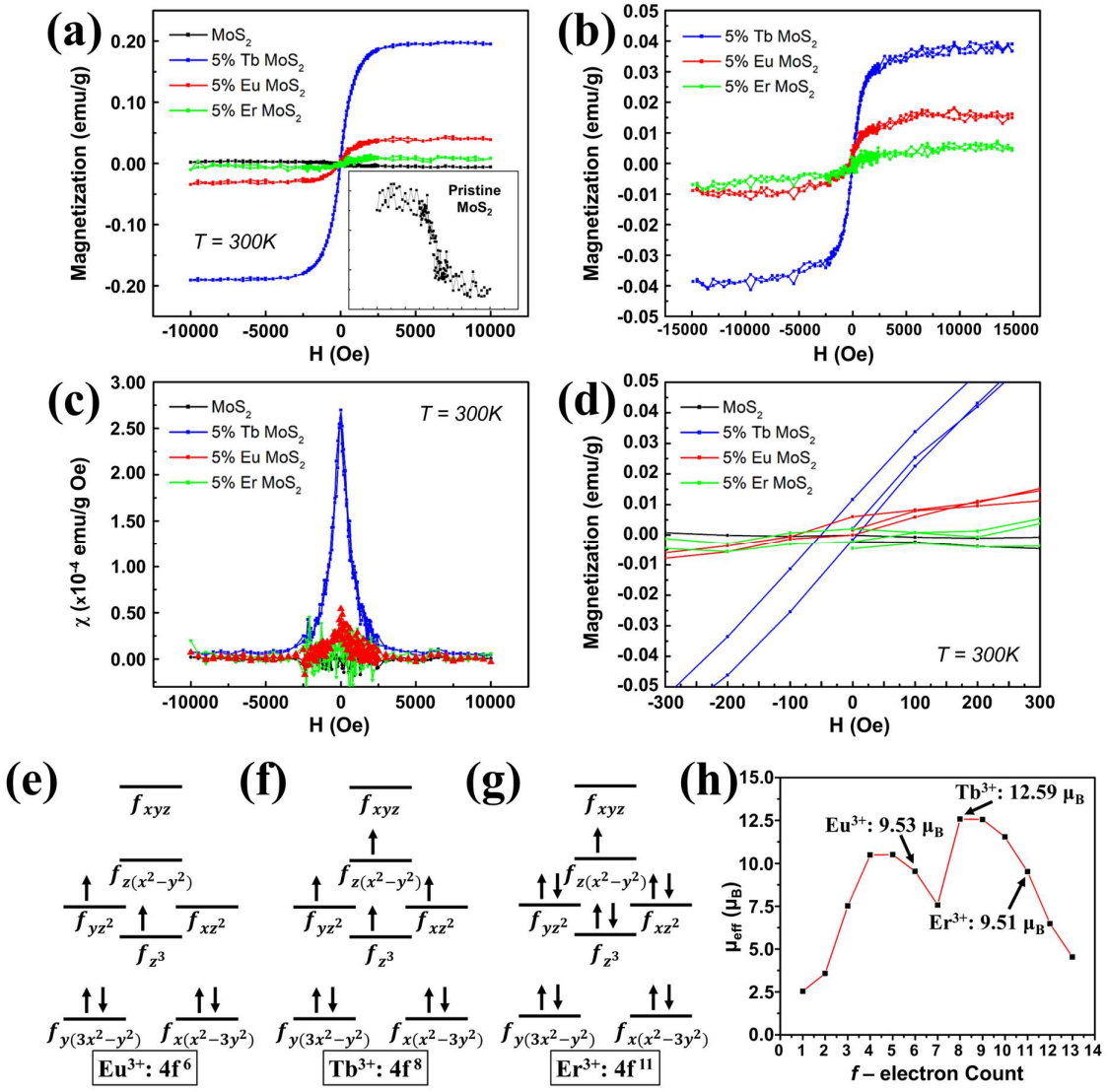

Figure 3. Magnetic characterization of dopant variable Ln-doped MoS_2 (Ln = Tb, Eu, Er) nanosheets. **(a)** M – H plot of Ln-doped MoS_2 nanosheets with different dopant ions (Ln = Tb, Eu, Er) at 5% atomic doping measured at room temperature, after correction of background paramagnetic contributions. **Inset**: Diamagnetic dominant signal from pristine MoS_2 nanosheet reference. **(b)** Comparative M – H plot of Ln-doped MoS_2 nanosheets (Ln = Tb^{3+}, Eu^{3+}, Er^{3+}) produced under more stringent annealing conditions, after correction against background paramagnetic signals. Comparison reveals the reproducible trend in dopant species influence and magnitude changes stemming from anneal condition stringency. **(c)** Corresponding susceptibility (χ – H) plot at room temperature (300K). **(d)** Enlarged low field region of the M – H plot within ±300 Oe, demonstrating minimal loop hysteresis in the measurements. **(e – h)** Proposed 4*f* electron distributions under crystal field (CF) splitting from a trigonal prismatic (D_{3h} symmetry) arrangement of surrounding sulphur atoms, for **(e)** Eu-doped MoS_2, **(f)** Tb-doped MoS_2 and **(g)** Er-doped MoS_2 nanosheets comprising Ln substitutional doping at Mo atomic sites. **(h)** Proposed trend of effective magnetic moment (μ_{eff}) across the 14 lanthanide ions, derived from spin-orbit interactions, under the crystal field influence proposed in **(e – g)**.

The magnetic performance of the MoS_2 nanosheets doped with various lanthanide ions was evaluated by vibrating sample magnetometry (VSM). Standardized across 5% doping concentrations, the nanosheets imbued with Tb^{3+}, Eu^{3+} and Er^{3+} demonstrated differing magnetization dependence in response to the external magnetic field **(Figure 3a)**. The ferromagnetic signals presented a trend of increasing magnetization values, whereby the sample doped with Tb^{3+} have the strongest magnetization, followed by Eu^{3+} then Er^{3+}. In contrast, pristine MoS_2 **(Figure 3a inset)** crafted via the same synthetic procedure presented distinct diamagnetic signal. Herein, it is imperative to note that the diamagnetic signature in the pristine MoS_2 nanosheets indicates that inherent defect-related magnetic origins (vacancy clusters, edges,[84,85] grain boundaries[86,87]) are significantly trivial in comparison to the effects brought about by rare earth doping. Besides, given that most rare earth oxides, even if present in trace quantities, are paramagnetic and not ferromagnetic at room temperature,[88,89] the observed ferromagnetic ordering should signal the importance of the dopants in altering the magnetic properties of the host. After brief omission of the ion paramagnetic contributions through linear extrapolation, the room temperature saturation magnetization at 10 kOe gave an impressive 0.1963 emu g^{-1} for 5% Tb^{3+} doping, while that for 5% Eu and 5% Er attained 0.0400 and 0.0078 emu g^{-1} respectively.

Beyond dopant dependence, the magnetic capabilities of the samples were also assessed in relation to the nanosheet quality. In a parallel study, a separate batch of nanosheets produced under identical experimental conditions except with greater stringency in the inert annealing process, yielded magnetic performance of uniformly reduced magnitudes **(Figure 3b)**. Under highly inert annealing conditions, the improved sample quality displayed inferior magnetic performance, indicating the critical role of potential defects such as sulphur vacancies (V_S) contributing to the overall magnetic performance. Here, it is noteworthy that despite the overall decrease in magnetization, the trend of dopant influence remains in the order of $Tb^{3+} > Eu^{3+} > Er^{3+}$, assuring reliability of the results acquired. Unsurprisingly, the derived susceptibility (χ – H) affiliation displays an identical trend of sample magnetizability in the order of $Tb^{3+} > Eu^{3+} > Er^{3+}$ **(Figure 3c; derived from Figure 3a)**, while a magnified examination of the M – H relation under low field (-300 Oe to 300 Oe) condition unveils lower coercivity, asserting a soft ferromagnetic character to the nanosheets **(Figure 3d; magnified from Figure 3a)**.

Simply through a preliminary correlation of the magnetization dependence upon dopant variation and sample quality, it is possible to ascribe the ferromagnetic origin to the formation of bound magnetic polarons (BMPs). The BMPs are typically evaluated in various DMS systems,[37,42,61] where polaron domains are created from ferromagnetic exchange between defect-localized carrier spins with vicinal magnetic ions. Since electron bound V_S defects have been known to be typically abundant in TMD nanostructures, the inclusion of lanthanide dopants is definite to produce BMPs from close radial proximity alignment of the lanthanide unpaired spins with the localized defect state. The hybridization of the dopant energy levels with the vacancy defect states effectively drives the ferromagnetic interactions between the Ln^{3+} dopant ions located within the polaron radius.[7] Therefore, the overall magnetization is expected to be directly proportion to the density of defects, as well as the magnetic moment of the dopant. Since lanthanide ion substitution at the Mo^{4+} sites was previously determined to be most thermodynamically favorable,[48] a proposed distribution of the *f*-electrons under the context of a D_{3h} trigonal prismatic crystal field[90,91] of S atoms was applied for each of the dopant ions (Tb^{3+}, Eu^{3+}, Er^{3+}) in **Figure 3e-g**. With a reasonable assignment of the crystal field

splitting, the overall effective magnetic moment was determined, taken into account spin-orbit coupling from the spin and unquenched orbital momentum contributions.[92–94] The resultant theoretical trend across the family of lanthanides **(Figure 3h)** was coherent with the experimental results, giving magnetization values in the order of $MoS_2:Tb^{3+}$ > $MoS_2:Eu^{3+}$ > $MoS_2:Er^{3+}$. Herein, it is noteworthy that the magnetic moments determined from **Figure 3h** should only adopt a qualitative relation to the actual moments measured; the theoretical derivation for magnetic moments (in μ_B/magnetic ion) should be less effective in quantifying non-conventional diluted magnetic systems involving coupling interactions between magnetic ions and localized defect states.

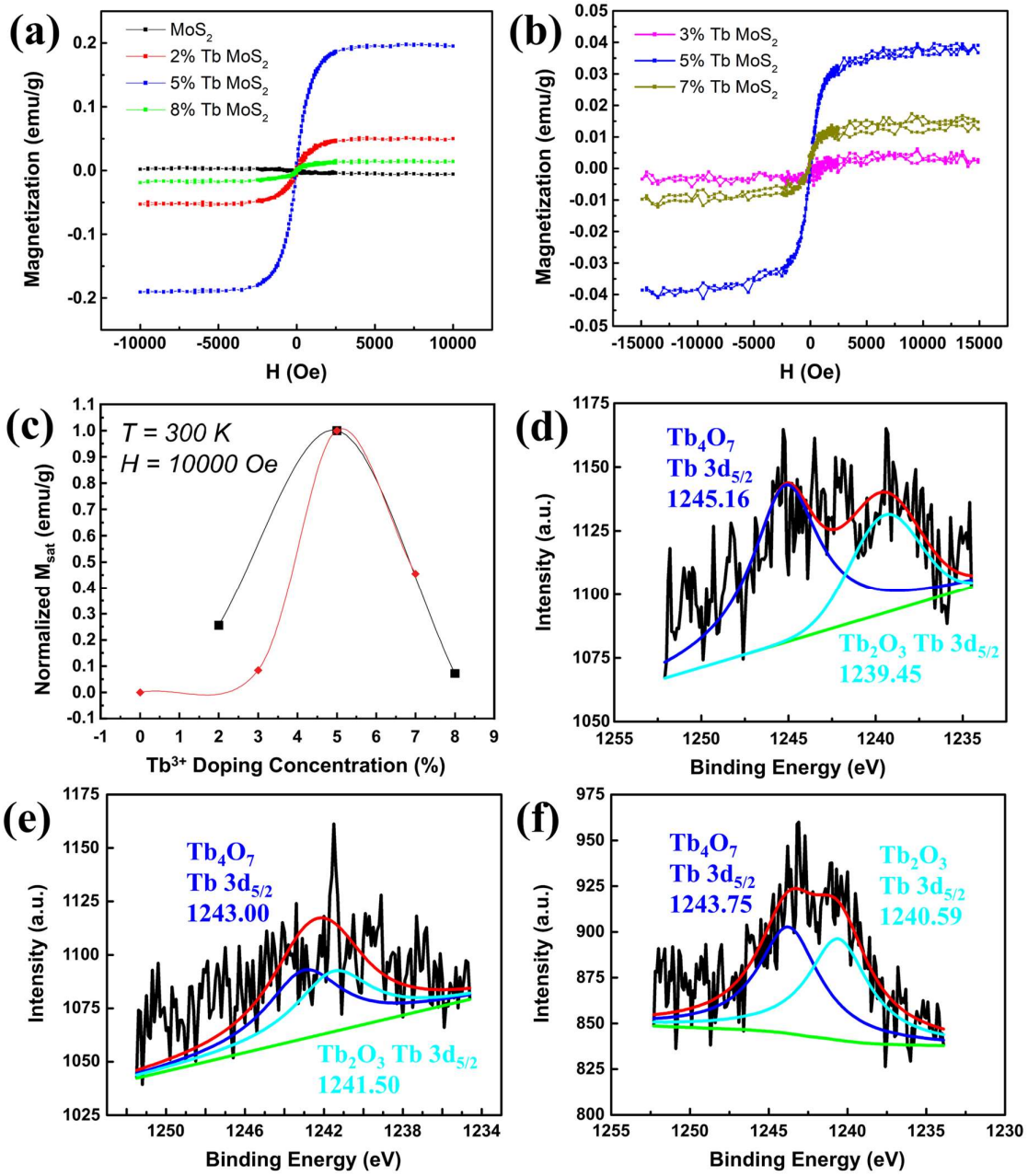

Figure 4. Magnetic characterization of Tb – MoS_2 nanosheets under variable atomic doping concentrations. (a) M – H plot for single batch Tb-doped MoS_2 nanosheets with 2%, 5% and 8% atomic doping concentrations, after correction of background paramagnetic contributions. **(b)** M – H plot for single batch Tb-doped MoS_2 nanosheets with 3%, 5% and 7% atomic doping concentrations, after correction of background paramagnetic contributions. **(c)** Normalized comparison of saturation magnetization across samples of various doping concentrations, demonstrating a parabolic relation optimal at 5% Tb doping. Values standardized at H = 10 kOe, black and red plot points refer to sample batches presented in **(a)** and **(b)** respectively, normalized against strongest magnetization in 5% Tb samples. **(d – f)** XPS characterization of Tb3d signals from **(d)** 5% Tb-doped MoS_2, **(e)** 7% Tb-doped MoS_2, **(f)** 8% Tb-doped MoS_2 nanosheets.

Owing to the strong ferromagnetic response from Tb-doped MoS_2 nanosheets, the correlation between dopant concentration and magnetic performance was investigated with Tb-doping (at.%) as the basis. Across two separate batches of Tb-doped samples, similar trends were sustained, with increasing magnetic response up to an optimal at 5% Tb-doping before a subsequent decline. The respective batches of nanosheets displayed magnetization trends in orders of 5% > 2% > 8% **(Figure 4a)** and 5% > 7% > 3% **(Figure 4b)**. Plotted together across a normalized scale, the comparative magnetization between the samples gave a reasonable correlation familiar to doped magnetic systems – a trending increment at low concentrations before a tapering decline beyond the optimal doping concentration **(Figure 4c)**. Similar trends (with maximum magnetic performance at 5% doping) were also observed for Er- and Eu doped samples when examined across 3%, 5% and 8% doping concentrations **(Figure S4)**. Naturally, with doping concentrations greater than the optimum, the decreased inter-ionic distance between these embedded foreign ions, and/or dopant clustering beyond the solid solubility limit, promoted antiferromagnetic coupling between adjacent dopants over the BMP ferromagnetic mechanism. The ferromagnetic performance is gradually compromised by the thermodynamically favored antiferromagnetic coupling, resulting in the progressive weakening of the ferromagnetic signal. Nonetheless, with consistent assignment of elemental signals for the Tb content under XPS analyses **(Figure 4d-f; full XPS data set under Figure S5)**, the lack of any new chemical states or clustering signals would indicate doping below the host solubility limit; the decreased magnetic ordering therefore stems merely from antiferromagnetic coupling at reduced Tb-Tb inter-ionic distances.

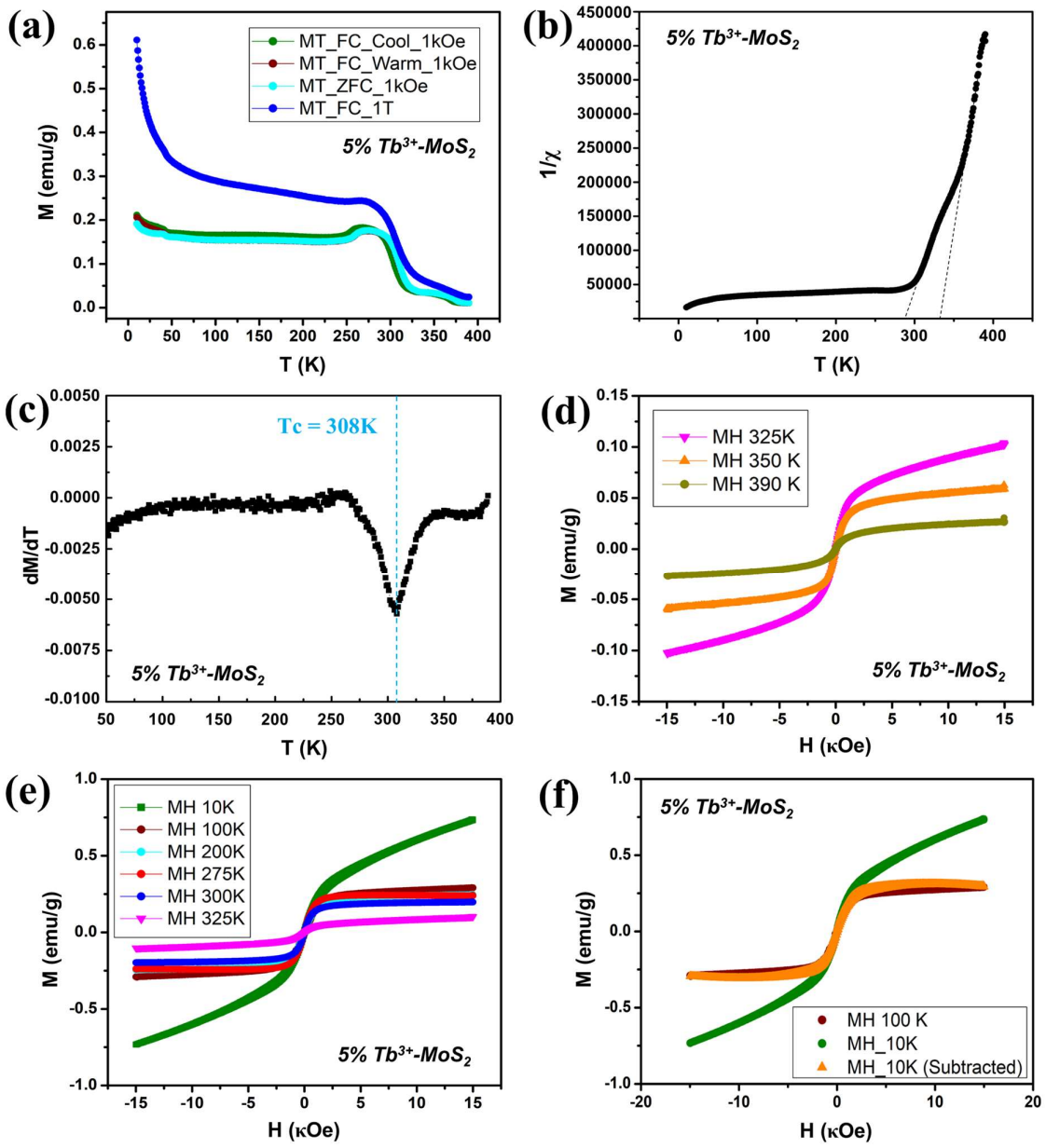

Figure 5. Temperature dependent magnetic characterization of 5% Tb-doped MoS_2 nanosheets. (a) M – T relation for 5% Tb-doped MoS_2 nanosheet under FC-warming, FC-cooling, FC-high field (1T) and ZFC measurement conditions. **(b)** 1/χ against T plot demonstrating ferromagnetic characteristics of the sample through positive x-intercepts. **(c)** Derivative dM/dT against T relation in determination of transition curie temperature (T_C) at approximately 308K. **(d)** M – H characteristics at high temperature domain of 325K, 350K and 390K. **(e)** M – H characteristics across low-intermediate temperature range from 10K to 325K. **(f)** M – H characteristics at low temperatures (10K, 100K) with processed plot (10K) upon paramagnetic subtraction.

Under temperature relation, the ferromagnetic feature of 5% Tb-doped MoS_2 sample was found to persist beyond room temperature. The unconventional shape of the M-T plot describes rich complex interplay of many different magnetic processes that can be deconvoluted in the subsequent analysis of individual M-H plots across different temperature points **(Figure 5a)**. The processed plot of 1/χ against T revealed magnetic transitions with extrapolated x-intercepts yielding positive values **(Figure 5b)**, assuring the ferromagnetic nature of these various

processes. The derivative spectrum of dM/dT against T further details a Curie transition temperature (T_C) at 308K **(Figure 5c)**, reaffirming the capability of these doped nanosheets as room temperature DMSs. Through a series of M-H spectra acquired across different temperature points, the systematic changes in magnetic features would allow holistic understanding of the magnetic transitions across the temperature scale. At higher temperatures ($T > T_C$) **(Figure 5d)**, there exists mixed strength of paramagnetic and ferromagnetic signals that increase marginally with decreasing temperature. Below Tc, the system transits into a ferromagnetic order, presenting a competitive ferromagnetic-antiferromagnetic interaction through a cusp feature between 250K and 300K, before stabilizing to a ferromagnetic state across a large temperature range down to 50K **(Figure 5a, 5e)**. At 10K, the spike in overall magnetization of the system is characterized by a paramagnetic or antiferromagnetic contribution in addition to the ferromagnetic feature, resulting in an unconventional upward curvature under both field-cooled (FC) and zero field-cooled (ZFC) conditions, with reduced bifurcation at low magnetization. Such a feature is expected to arise from an inherent low temperature response coming from the Tb dopants or MoS_2 host.[77,85] Subtracted of the background linear contribution through extrapolation, the resultant ferromagnetic signal was compared against the next acquired data-point at 100K, revealing minimal changes in the ferromagnetic feature in certainty that the overall increased magnetization stems purely from the additional linear magnetic component **(Figure 5f)**.

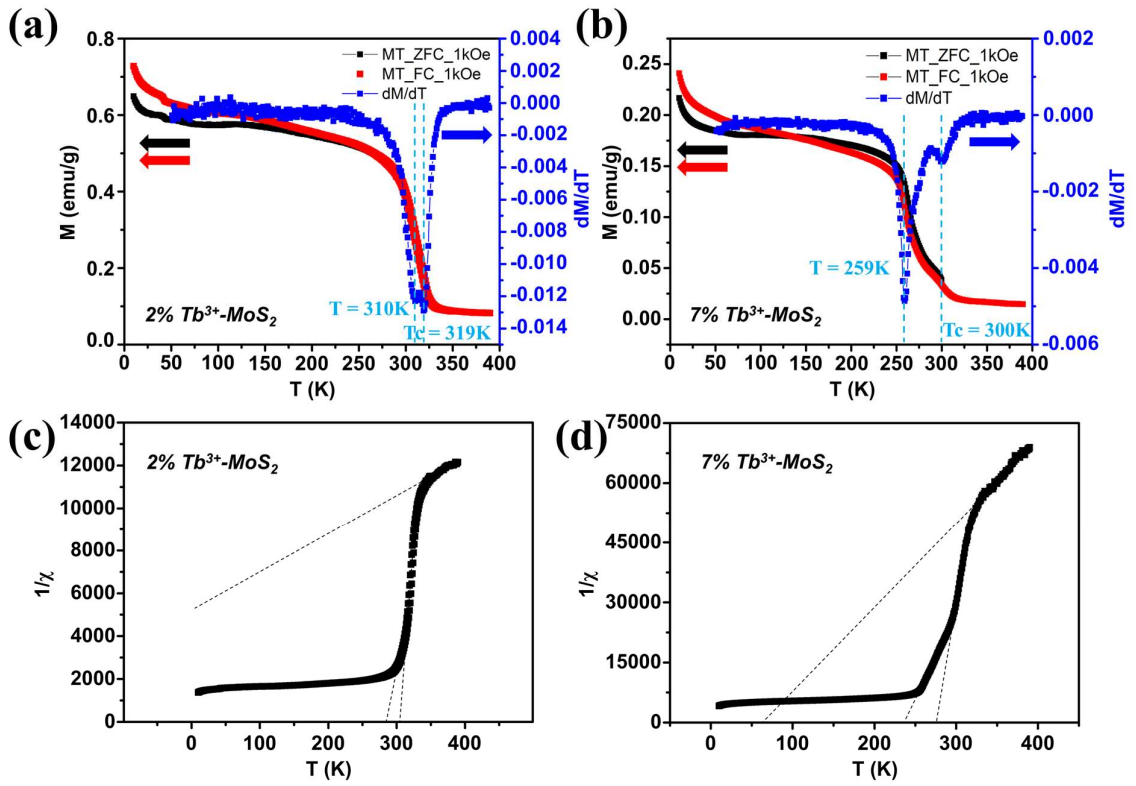

Figure 6. Temperature dependent magnetic characterization of 2% and 7% Tb-doped MoS_2 nanosheets. (a, b) Respective M – T relations (red and black) for 2% and 7% Tb-doped MoS_2 nanosheet under FC-ZFC measurement conditions, overlaid with the derivative dM/dT against T relations (blue) in determination of transition Curie temperatures (T_C) for the respective samples: 319K for 2% Tb-doped sample (with side transition at 310K); 300K for 7% Tb-doped sample (with side transition at 259K). **(c, d)** Corresponding $1/\chi$ against T plots demonstrating magnetic transition characteristics of the samples through x-intercepts.

In comparison, the M-T relations for the 2% and 7% Tb-doped samples were found to feature similar plot morphologies **(Figure 6a, b; red and black)**, with the 2% Tb-doped sample featuring a T_C at approximately 319K, while the 7% Tb-doped sample has a T_C value of 300K along with a separate ferromagnetic transition at the onset of 259K. **(Figure 6a, b; blue)**. Once again, the consistent positive x-intercepts in the $1/\chi$ plots reiterates the ferromagnetic transitions involved **(Figure 6c, d)**. Plotted upon a common scale, the relation between the ascribed T_C and Tb-dopant concentration presented a linear plot of inverse relation **(Figure S6)**.

3.3. Bound Magnetic Polaron Modelling

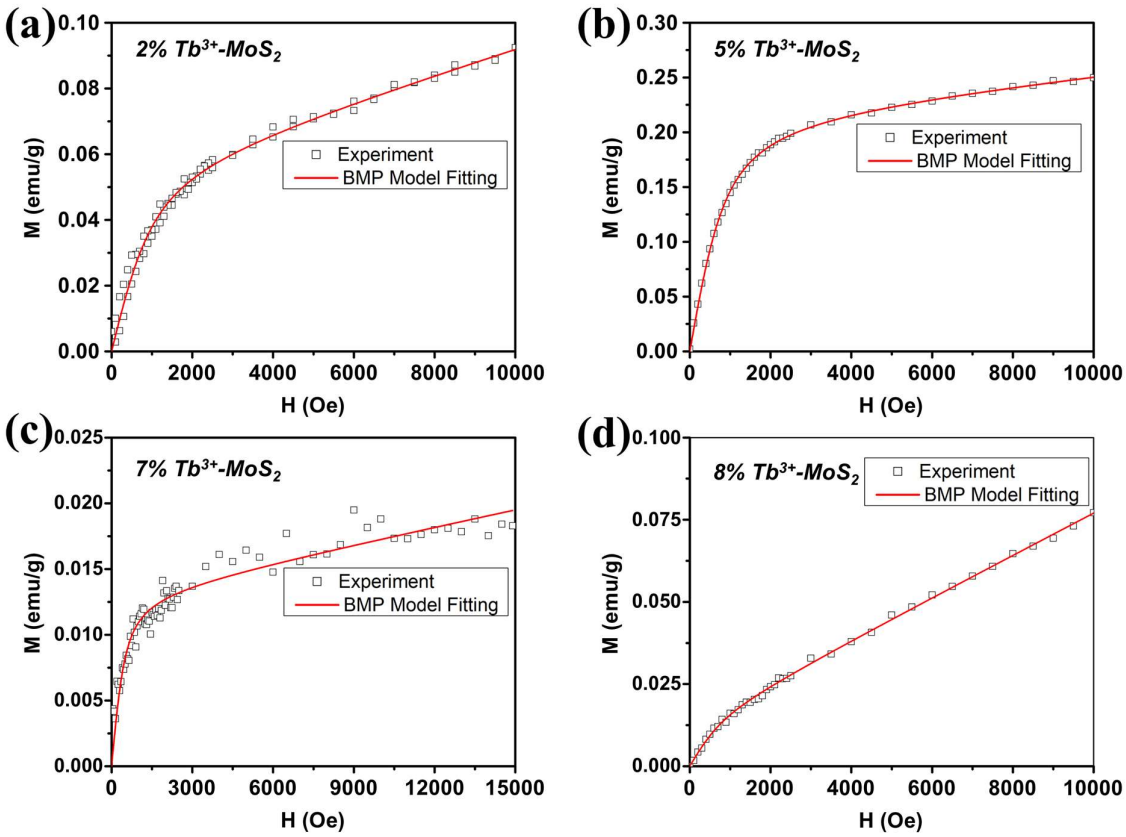

Figure 7. BMP model fitting of initial M-H relation for Tb-Doped MoS_2 sample at different atomic doping concentrations. (a) 2% Tb-doping. **(b)** 5% Tb-doping. **(c)** 7% Tb-doping. **(d)** 8% Tb-doping.

In further evaluation of the BMP model in describing the observed ferromagnetic trends, the initial onsets of the M-H plots were fitted in accordance with the following relation

$$M = M_0 L(x) + \chi_m H$$

where the first term models upon magnetic contributions from the BMPs while the second term relates to paramagnetic contributions from the host matrix. The overall magnetization, $M_0 = Nm_s/\rho$, where m_s is the moment per BMP, N refers to the number of BMPs per unit volume and ρ is the density of host matrix (ρ(MoS_2) = 5.06 g cm^{-3}). $L(x) = \coth(x) - 1/x$ is the Langevin function with $x = Hm_{eff}/k_BT$, where m_{eff} is the effective moment per BMP. Ignoring the interactions between the BMPs, an approximation for $m_s = m_{eff}$ allows for determination of variables M_0, m_{eff} and χ_m from the equation fit. As displayed in **Figure 7** and **Figure S7**, the apropos fits detailed by quality modelling statistics **(Figure S8, S9; reduced χ^2 at 10^{-6} to 10^{-8})** were committed for the M-H plots under the respective variations in dopant concentrations and temperature. The parameters derived from the various plots are summarized under **Table 1**.

Table 1. Magnetization Parameters (M_0, m_{eff}, χ_m, N) Derived from BMP Model Fitting for Tb-doped Samples under Varied Dopant Concentrations (2%, 5%, 7%, 8%), and 5% Tb-doped Sample under Temperature Variation.

Dopant Conc. (%Tb^{3+})	M_0 (emu/g)	m_{eff} (emu)	χ_m (emu/g·Oe)	N (cm^{-3})
2	0.056	1.0×10^{-16}	3.8×10^{-6}	2.8×10^{15}
5	0.219	1.2×10^{-16}	3.9×10^{-6}	9.6×10^{15}
7	0.013	2.0×10^{-16}	6.4×10^{-6}	3.3×10^{14}
8	0.014	1.3×10^{-16}	4.3×10^{-7}	5.3×10^{14}

Temperature (K)	M_0 (emu/g)	m_{eff} (emu)	χ_m (emu/g·Oe)	N (cm^{-3})
10	0.352	2.5×10^{-18}	2.7×10^{-5}	7.2×10^{17}
100	0.277	2.8×10^{-17}	1.4×10^{-6}	5.0×10^{16}
200	0.255	6.7×10^{-17}	3.3×10^{-7}	1.9×10^{16}
275	0.268	1.2×10^{-16}	1.6×10^{-6}	1.1×10^{16}
300	0.195	1.4×10^{-16}	4.1×10^{-7}	6.9×10^{15}
325	0.065	1.0×10^{-16}	2.7×10^{-6}	3.3×10^{15}
350	0.047	1.5×10^{-16}	8.7×10^{-7}	1.6×10^{15}
390	0.020	9.8×10^{-17}	5.4×10^{-7}	1.0×10^{15}

The extracted values for effective BMP moments were in the order of 10^{-16} emu, adopting a general trend of marginal increment with increasing dopant content. Precluding any counteracting antiferromagnetic contributions, the above-mentioned correlation is expected to present a reasonable trend, in which the increased dopant count homogeneously elevates the density of magnetic dopant within the BMP radius, enhancing the magnetic moment of individual BMPs. Considering within batch samples, the relation of 2%, 5% and 8% doping demonstrated a linear trend against m_{eff} **(Figure 8a)**. In contrast, the sample densities of BMPs were found in orders of 10^{14} – 10^{15} BMPs per cm^3, with an inverse relation to the increasing dopant concentrations. The resultant trend adopts the same curvature as the overall sample magnetization **(Figure 8b)**, having an optimal value at 5% doping before a subsequent decline with higher concentrations. The matrix paramagnetic susceptibilities revealed low influence from the host material, exerting non-trending values on the order of 10^{-6} emu/g·Oe.

With temperature variation, the samples accommodated higher density of BMPs at lower temperatures, from 1.0×10^{15} BMPs/cm^3 at 390K up to 7.2×10^{17} BMPs/cm^3 at 10K through a trend approximated by a $(1 + x)^{-1.3}$ relation **(Figure 8c)**. It may be reasonable to accord the reduced BMP count towards greater instability when faced with increased thermal disruptions at higher temperatures. The polarons were ascribed with effective magnetic moments that generally rise with temperature for values below T_C, having 2.5×10^{-18} emu at 10K and $1.4 \times 10^{-}$

^{16} emu at 300K. The trending order within this temperature range could be approximated by a cubic function **(Figure 8d, trending statistics in Figure S10)**. Beyond T_C, the values do not accord with a proper trend owing to the interplay of additional magnetic (paramagnetic, antiferromagnetic) contributions.

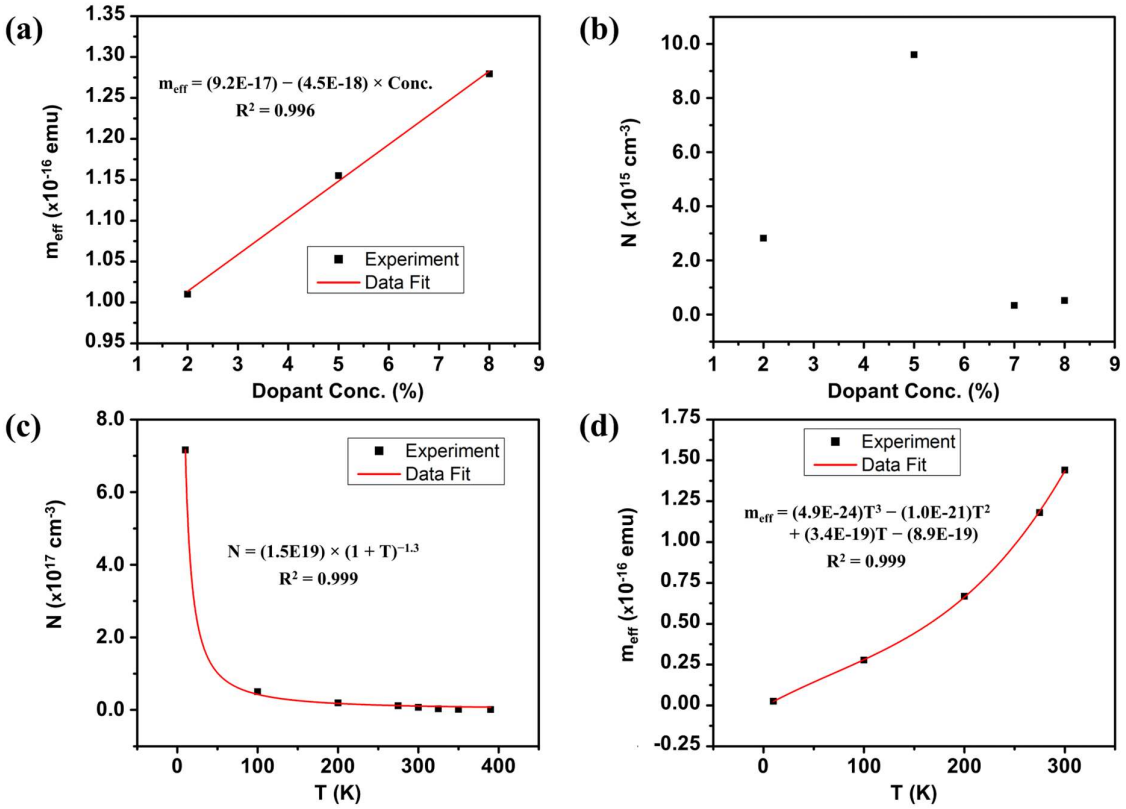

Figure 8. Relation of BMP model derived parameters to Tb doping concentrations and temperature influence. (a) Dependence of effective magnetic moment per BMP (m_{eff}) on Tb doping concentrations, together with associated model fitting details. **(b)** BMP density (N) relation to Tb doping concentrations. **(c)** Variation in density of BMPs (N) within the sample in relation to temperature changes, together with associated model fitting details. **(d)** Variation in effective magnetic moment per BMP (m_{eff}) depending on measurement temperature conditions, together with associated model fitting details.

4. Conclusions

With disparate lanthanide dopants (Ln = Tb, Eu, Er), doped MoS_2 nanosheets were produced in assessment of its various magnetic performances. The effective trend across consistently doped (5%) samples afforded magnetization in order of $Tb^{3+} > Eu^{3+} > Er^{3+}$, justified by the consolidation of possible mechanistic contributions coming from crystal field influence and BMPs. With Tb-doped MoS_2 systems as the basis of study, the dependence of sample magnetic response upon dopant concentration was evaluated, presenting a trend of low concentration increase before a subsequent decline beyond the optimal doping threshold. Such observation could be accountable through competing interplay between ferromagnetic and antiferromagnetic processes at work, resulting in acquired modulation of sample magnetization simply through doping proportions. The dependency of magnetization against doping ratios and annealing conditions, along with apropos modelling of M-H relations under the BMP model, served to strengthen the notion of BMP production contributing to room temperature ferromagnetic properties. These findings are expected to cater further insights into the scarce experimental studies on rare earth doped MoS_2 systems, highlighting the potential of lanthanide doped nanosheets for spintronic and magnetic applications.

Author Contributions

Eng Tuan Poh – Conceptualization, Investigation, Formal Analysis, Methodology, Validation, Data Curation, Visualization, Writing – Original Draft; **Rajasree Das** – Investigation, Formal Analysis, **Manikandan Marimuthu** – Investigation, Formal Analysis; **Zheng Zhang** – Investigation, Formal Analysis; **Ramanathan Mahediran** – Funding Acquisition, Project Administration, Supervision, Writing – Review & Editing; **Chorng Haur Sow** – Funding Acquisition, Project Administration, Supervision, Writing – Review & Editing.

Acknowledgements

Our gratitude to Dr. Chen Yun and Dr. Zhao Fangfang from Bruker, along with Dr. Wang Xinyun, for the advice on Magnetic Force Microscopy (MFM) attempted for this project.

Conflict of Interest

The authors declare no conflict of interest.

References

[1] T. Dietl, H. Ohno, F. Matsukura, *Phys. Rev. B - Condens. Matter Mater. Phys.* **2001**, *63*, 195205. DOI 10.1103/PhysRevB.63.195205.

[2] T. Dietl, H. Ohno, F. Matsukura, J. Cibert, D. Ferrand, *Science (80-.).* **2000**, *287*, 1019.

[3] J. B. Torrance, M. W. Shafer, T. R. McGuire, *Phys. Rev. Lett.* **1972**, *29*, 1168.

[4] M. Nawrocki, R. Planel, G. Fishman, R. Galazka, *Phys. Rev. Lett.* **1981**, *46*, 735.

[5] T. Dietl, J. Spałek, *Phys. Rev. B* **1983**, *28*, 1548.

[6] D. Heiman, P. A. Wolff, J. Warnock, *Phys. Rev. B* **1983**, *27*, 4848.

[7] J. M. D. Coey, M. Venkatesan, C. B. Fitzgerald, *Nat. Mater.* **2005**, *4*, 173.

[8] T. Dietl, *Phys. Rev. Lett.* **2023**, 130, 086202.

[9] M. Wu, X. Yao, Y. Hao, H. Dong, Y. Cheng, H. Liu, F. Lu, W. Wang, K. Cho, W. H. Wang, *Phys. Lett. Sect. A Gen. At. Solid State Phys.* **2018**, *382*, 111.

[10] C. Jia, B. Zhou, Q. Song, X. Zhang, Z. Jiang, *RSC Adv.* **2018**, *8*, 18837.

[11] A. A. Tedstone, D. J. Lewis, P. O'Brien, *Chem. Mater.* **2016**, *28*, 1965.

[12] A. Yoshimura, N. Koratkar, V. Meunier, *Nano Express* **2020**, *1*, 010008.

[13] T. H. Nhung, R. Planel, C. Benoit, L. Guillaume, A. K. Bhattacharjee, *Phys. Rev. B* **1985**, *31*, 2388.

[14] P. A. Wolff, J. Warnock, *J. Appl. Phys.* **1984**, *55*, 2300.

[15] S. Jaiswar, K. D. Mandal, *J. Phys. Chem. C* **2017**, *121*, 19586.

[16] P. Senthilkumar, S. Dhanuskodi, J. Karthikeyan, P. Murugan, *Phys. Chem. Chem. Phys.* **2019**, *21*, 4032.

[17] A. Bandyopadhyay, S. Sutradhar, B. J. Sarkar, A. K. Deb, P. K. Chakrabarti, *Appl. Phys. Lett.* **2012**, *100*, 252411. DOI 10.1063/1.4729386.

[18] N. Bhakta, T. Inamori, R. Shirakami, Y. Tanioku, K. Yoshimura, P. K. Chakrabarti, *Mater. Res. Bull.* **2018**, *104*, 6.

[19] S. Banerjee, K. Rajendran, N. Gayathri, M. Sardar, S. Senthilkumar, V. Sengodan, *J. Appl. Phys.* **2008**, *104*, 043913. DOI 10.1063/1.2969945.

[20] W. Q. Zou, C. N. Ge, G. Venkataiah, H. L. Su, H. S. Hsu, J. C. A. Huang, X. C. Liu, F. M. Zhang, Y. W. Du, *J. Appl. Phys.* **2012**, *111*, 113704. DOI 10.1063/1.4720381.

[21] A. Franco, H. V. S. Pessoni, M. P. Soares, *J. Magn. Magn. Mater.* **2014**, *355*, 325.

[22] P. R. Chithira, T. Theresa John, *J. Magn. Magn. Mater.* **2020**, *496*, 165928.

[23] L. T. Tseng, A. Suter, Y. R. Wang, F. X. Xiang, P. Bian, X. Ding, A. Tseng, H. L. Hu, H. M. Fan, R. K. Zheng, X. L. Wang, Z. Salman, T. Prokscha, K. Suzuki, R. Liu, S. Li, E. Morenzoni, J. B. Yi, *Phys. Rev. B* **2017**, *96*, 104423.

[24] D. C. Agarwal, U. B. Singh, S. Gupta, R. Singhal, P. K. Kulriya, F. Singh, A. Tripathi,

J. Singh, U. S. Joshi, D. K. Avasthi, *Sci. Rep.* **2019**, *9*, 6675.

[25] P. Robkhob, I. M. Tang, S. Thongmee, *Mater. Sci. Eng. B Solid-State Mater. Adv. Technol.* **2020**, *260*, 114644.

[26] P. Kaur, Kriti, Rahul, S. Chalotra, H. Kaur, A. Kandasami, D. P. Singh, *Appl. Surf. Sci. Adv.* **2021**, *5*, 100100.

[27] E. Z. Xu, H. M. Liu, K. Park, Z. Li, Y. Losovyj, M. Starr, M. Werbianskyj, H. A. Fertig, S. X. Zhang, *Nanoscale* **2017**, *9*, 3576.

[28] R. Mishra, W. Zhou, S. J. Pennycook, S. T. Pantelides, J. C. Idrobo, *Phys. Rev. B - Condens. Matter Mater. Phys.* **2013**, *88*, 144409.

[29] J. Wang, F. Sun, S. Yang, Y. Li, C. Zhao, M. Xu, Y. Zhang, H. Zeng, *Appl. Phys. Lett.* **2016**, *109*, 092401.

[30] A. Ramasubramaniam, D. Naveh, *Phys. Rev. B - Condens. Matter Mater. Phys.* **2013**, *87*, 195201.

[31] X. Zhao, C. Xia, T. Wang, X. Dai, *Solid State Commun.* **2015**, *220*, 31.

[32] S. Fu, K. Kang, K. Shayan, A. Yoshimura, S. Dadras, X. Wang, L. Zhang, S. Chen, N. Liu, A. Jindal, X. Li, A. N. Pasupathy, A. N. Vamivakas, V. Meunier, S. Strauf, E. H. Yang, *Nat. Commun.* **2020**, *11*, 6.

[33] H. Shu, P. Luo, P. Liang, D. Cao, X. Chen, *ACS Appl. Mater. Interfaces* **2015**, *7*, 7534.

[34] Z. Chen, J. He, P. Zhou, J. Na, L. Z. Sun, *Comput. Mater. Sci.* **2015**, *110*, 102.

[35] Z. C. Xiang, Z. Zhang, X. J. Xu, Q. Zhang, Q. B. Wang, C. Yuan, *Phys. Chem. Chem. Phys.* **2015**, *17*, 15822.

[36] Y. Wang, S. Li, J. Yi, *Sci. Rep.* **2016**, *6*, 24153.

[37] H. Duan, P. Guo, C. Wang, H. Tan, W. Hu, W. Yan, C. Ma, L. Cai, L. Song, W. Zhang, Z. Sun, L. Wang, W. Zhao, Y. Yin, X. Li, S. Wei, *Nat. Commun.* **2019**, *10*, 1584.

[38] J. Zhou, J. Lin, H. Sims, C. Jiang, C. Cong, J. A. Brehm, Z. Zhang, L. Niu, Y. Chen, Y. Zhou, Y. Wang, F. Liu, C. Zhu, T. Yu, K. Suenaga, R. Mishra, S. T. Pantelides, Z. G. Zhu, W. Gao, Z. Liu, W. Zhou, *Adv. Mater.* **2020**, *32*, 1906536.

[39] W. S. Yun, J. D. Lee, *Phys. Chem. Chem. Phys.* **2014**, *16*, 8990.

[40] A. M. Hu, L. L. Wang, W. Z. Xiao, B. Meng, *Phys. E Low-Dimensional Syst. Nanostructures* **2015**, *73*, 69.

[41] X. Sun, J. Dai, Y. Guo, C. Wu, F. Hu, J. Zhao, X. Zeng, Y. Xie, *Nanoscale* **2014**, *6*, 8359.

[42] W. Hu, H. Tan, H. Duan, G. Li, N. Li, Q. Ji, Y. Lu, Y. Wang, Z. Sun, F. Hu, C. Wang, W. Yan, *ACS Appl. Mater. Interfaces* **2019**, *11*, 31155.

[43] Y. T. H. Pham, M. Liu, V. O. Jimenez, Z. Yu, V. Kalappattil, F. Zhang, K. Wang, T. Williams, M. Terrones, M. H. Phan, *Adv. Mater.* **2020**, *32*, 2003607.

[44] S. J. Yun, D. L. Duong, D. M. Ha, K. Singh, T. L. Phan, W. Choi, Y. M. Kim, Y. H.

Lee, *Adv. Sci.* **2020**, *7*, 1903076.

[45] F. Zhang, B. Zheng, A. Sebastian, D. H. Olson, M. Liu, K. Fujisawa, Y. T. H. Pham, V. O. Jimenez, V. Kalappattil, L. Miao, T. Zhang, R. Pendurthi, Y. Lei, A. L. Elias, Y. Wang, N. Alem, P. E. Hopkins, S. Das, V. H. Crespi, M. H. Phan, M. Terrones, *Adv. Sci.*, **2020**, 7, 2001174.

[46] W. Hu, H. Tan, H. Duan, G. Li, N. Li, Q. Ji, Y. Lu, Y. Wang, Z. Sun, F. Hu, C. Wang, W. Yan, *ACS Appl. Mater. Int.* **2019**, 11, 31155.

[47] A. Majid, A. Imtiaz, M. Yoshiya, *J. Appl. Phys.* **2016**, *120*, 142124. DOI 10.1063/1.4963380.

[48] C. N. M. Ouma, S. Singh, K. O. Obodo, G. O. Amolo, A. H. Romero, *Phys. Chem. Chem. Phys.* **2017**, *19*, 25555.

[49] Y. Lyu, Z. Wu, W. F. Io, J. Hao, *Appl. Phys. Lett.* **2019**, *115*, 153105. DOI 10.1063/1.5120173.

[50] G. Bai, S. Yuan, Y. Zhao, Z. Yang, S. Y. Choi, Y. Chai, S. F. Yu, S. P. Lau, J. Hao, *Adv. Mater.* **2016**, *28*, 7472.

[51] Y. Yang, H. Pu, J. Di, Y. Zang, S. Zhang, C. Chen, *Scr. Mater.* **2018**, *152*, 64.

[52] G. Bai, Z. Yang, H. Lin, W. Jie, J. Hao, *Nanoscale* **2018**, *10*, 9261.

[53] G. Bai, Y. Lyu, Z. Wu, S. Xu, J. Hao, *Sci. China Mater.* **2020**, *63*, 575.

[54] D. Xu, W. Chen, M. Zeng, H. Xue, Y. Chen, X. Sang, Y. Xiao, T. Zhang, R. R. Unocic, K. Xiao, L. Fu, *Angew. Chemie* **2018**, *130*, 763.

[55] J. Liu, R. Van Deun, A. M. Kaczmarek, *J. Mater. Chem. C* **2016**, *4*, 9937.

[56] M. Meng, X. Ma, *Nanoscale Res. Lett.* **2016**, *11*, 3.

[57] W. Shi, Z. Li, L. Wang, S. Wu, G. Zhang, M. Meng, X. Ma, *Opt. Commun.* **2018**, *406*, 50.

[58] X. Ding, X. Cui, A. Sohail, P. P. Murmu, J. Kennedy, N. Bao, J. Ding, R. Liu, M. Peng, L. Wang, X. Chu, A. Vinu, S. P. Ringer, J. Yi, *Adv. Quantum Technol.*, **2020**, 4, 2000093.

[59] Q. Zhao, Q. Lu, Y. Liu, M. Zhang, *Appl. Surf. Sci.* **2019**, *471*, 118.

[60] X. Chen, Z. Z. Lin, *J. Nanoparticle Res.* **2018**, *20*, 129.

[61] Q. Zhao, C. Zhai, Q. Lu, M. Zhang, *Phys. Chem. Chem. Phys.* **2019**, *21*, 232.

[62] C. Liu, H. Chen, S. Wang, Q. Liu, Y. G. Jiang, D. W. Zhang, M. Liu, P. Zhou, *Nat. Nanotechnol.* **2020**, *15*, 545.

[63] D. Akinwande, C. Huyghebaert, C. H. Wang, M. I. Serna, S. Goossens, L. J. Li, H. S. P. Wong, F. H. L. Koppens, *Nature* **2019**, *573*, 507.

[64] H. Wang, L. Yu, Y. H. Lee, Y. Shi, A. Hsu, M. L. Chin, L. J. Li, M. Dubey, J. Kong, T. Palacios, *Nano Lett.* **2012**, *12*, 4674.

[65] G. Fiori, F. Bonaccorso, G. Iannaccone, T. Palacios, D. Neumaier, A. Seabaugh, S. K. Banerjee, L. Colombo, *Nat. Nanotechnol.* **2014**, *9*, 768.

[66] T. Carey, S. Cacovich, G. Divitini, J. Ren, A. Mansouri, J. M. Kim, C. Wang, C. Ducati, R. Sordan, F. Torrisi, *Nat. Commun.* **2017**, *8*, 1202. DOI 10.1038/s41467-017-01210-2.

[67] T. Carey, A. Arbab, L. Anzi, H. Bristow, F. Hui, S. Bohm, G. Wyatt-Moon, A. Flewitt, A. Wadsworth, N. Gasparini, J. M. Kim, M. Lanza, I. McCulloch, R. Sordan, F. Torrisi, *Adv. Electron. Mater.* **2021**, *7*, 2100112

[68] F. Torrisi, T. Hasan, W. Wu, Z. Sun, A. Lombardo, T. S. Kulmala, G. W. Hsieh, S. Jung, F. Bonaccorso, P. J. Paul, D. Chu, A. C. Ferrari, *ACS Nano* **2012**, *6*, 2992.

[69] S. Conti, L. Pimpolari, G. Calabrese, R. Worsley, S. Majee, D. K. Polyushkin, M. Paur, S. Pace, D. H. Keum, F. Fabbri, G. Iannaccone, M. Macucci, C. Coletti, T. Mueller, C. Casiraghi, G. Fiori, *Nat. Commun.* **2020**, *11*, 3566.

[70] M. Sivan, Y. Li, H. Veluri, Y. Zhao, B. Tang, X. Wang, E. Zamburg, J. F. Leong, J. X. Niu, U. Chand, A. V. Y. Thean, *Nat. Commun.* **2019**, *10*, 5201.

[71] J. Jiang, K. Parto, W. Cao, K. Banerjee, *IEEE J. Electron Devices Soc.* **2019**, *7*, 878.

[72] S. Y. Seo, J. Park, J. Park, K. Song, S. Cha, S. Sim, S. Y. Choi, H. W. Yeom, H. Choi, M. H. Jo, *Nat. Electron.* **2018**, *1*, 512.

[73] Z. Hu, Y. Bao, Z. Li, Y. Gong, R. Feng, Y. Xiao, X. Wu, Z. Zhang, X. Zhu, P. M. Ajayan, Z. Fang, *Sci. Bull.* **2017**, *62*, 16.

[74] H. Li, Q. Zhang, C. C. R. Yap, B. K. Tay, T. H. T. Edwin, A. Olivier, D. Baillargeat, *Adv. Funct. Mater.* **2012**, *22*, 1385.

[75] C. H. Chang, S. S. Chan, *J. Catal.* **1981**, *72*, 139.

[76] L. Cai, J. He, Q. Liu, T. Yao, L. Chen, W. Yan, F. Hu, Y. Jiang, Y. Zhao, T. Hu, Z. Sun, S. Wei, *J. Am. Chem. Soc.* **2015**, *137*, 2622.

[77] R. Sanikop, C. Sudakar, *ACS Appl. Nano Mater.* **2020**, *3*, 576.

[78] C. Zhu, C. Lv, M. Jiang, J. Zhou, D. Li, X. Ma, D. Yang, *Appl. Phys. Lett.* **2016**, *108*, 051113. DOI 10.1063/1.4941430.

[79] M. Glätzle, O. Janka, V. Svitlyk, D. Chernyshov, M. Bartsch, H. Zacharias, R. Pöttgen, H. Huppertz, *Chem. - A Eur. J.* **2018**, *24*, 15236.

[80] D. D. Sarma, C. N. R. Rao, *J. Electron Spectros. Relat. Phenomena* **1980**, *20*, 25.

[81] M. A. Farid, H. Zhang, A. Yang, G. Tian, M. Wu, G. Li, F. Liao, J. Lin, *Eur. J. Inorg. Chem.* **2017**, *2017*, 1427.

[82] H. Li, W. Li, S. Gu, F. Wang, H. Zhou, *Catal. Sci. Technol.* **2016**, *6*, 3510.

[83] C. J. Lee, A. Sayal, S. Vashishtha, J. F. Weaver, *Phys. Chem. Chem. Phys.* **2019**, *22*, 379.

[84] W. Zhou, M. Chen, M. Guo, A. Hong, T. Yu, X. Luo, C. Yuan, W. Lei, S. Wang, *Nano Lett.* **2020**, *20*, 2923.

[85] D. Gao, M. Si, J. Li, J. Zhang, Z. Zhang, Z. Yang, D. Xue, *Nanoscale Res. Lett.* **2013**, *8*, 129.

[86] N. Gao, Y. Guo, S. Zhou, Y. Bai, J. Zhao, *J. Phys. Chem. C* **2017**, *121*, 12261.

[87] Z. Zhang, X. Zou, V. H. Crespi, B. I. Yakobson, *ACS Nano* **2013**, *7*, 10475.

[88] J. B. Maccheskey, H. J. Williams, R. C. Sherwood, J. F. Potter, *J. Chem. Phys.* **1966**, *44*, 596.

[89] K. Trepka, Y. Tao, *Appl. Phys. Lett.* **2020**, *117*, 122410. DOI 10.1063/5.0023466.

[90] M. Ju, X. Kuang, C. Lu, H. Li, J. Wang, C. Zhang, Y. Zhu, Y. Yeung, *J. Mater. Chem. C* **2016**, *4*, 1988.

[91] W. W. Lukens, M. Speldrich, P. Yang, T. J. Duignan, J. Autschbach, P. Kögerler, *Dalt. Trans.* **2016**, *45*, 11508.

[92] J. H. Van Vleck, A. Frank, *Phys. Rev.* **1929**, *34*, 1494.

[93] B. Wang, S. Jiang, X. Wang, S. Gao, *Sci. China, Ser. B Chem.* **2009**, *52*, 1739.

[94] L. Sorace, D. Gatteschi, *Lanthanides Actinides Mol. Magn.* **2015**, *2*, 1.